TECHNICAL RESEARCH REPORT

Dynamics of Neural Responses in Ferret Primary Auditory Cortex: I. Spectro-Temporal Response Field Characterization by Dynamic Ripple Spectra

by D.A. Depireux, J.Z. Simon, D.J. Klein, S.A. Shamma

CAAR T.R. 99-3
(ISR T.R. 99-62)

The Center for Auditory and Acoustic Research (CAAR) is a consortium of researchers from six universities working in partnership with Department of Defense laboratories and industry. CAAR is funded by the Office of Naval Research through a 1997 Department of Research Initiative.

Web site http://www.isr.umd.edu/CAAR/

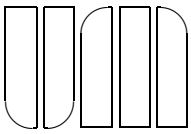

Dynamics of Neural Responses in Ferret Primary Auditory Cortex: I. Spectro-Temporal Response Field Characterization by Dynamic Ripple Spectra

Didier A. Depireux[*] Jonathan Z. Simon[*] David J. Klein [*†] and Shihab A. Shamma[*†]

[*]*Institute for Systems Research*
[†]*Department of Electrical and Computer Engineering*
University of Maryland
College Park MD 20742–3311, USA
(301) 405-6596

Abstract

To understand the neural representation of broadband, dynamic sounds in Primary Auditory Cortex (AI), we characterize responses using the Spectro-Temporal Response Field (STRF). The STRF describes and predicts the linear response of neurons to sounds with rich spectro-temporal envelopes. It is calculated here from the responses to elementary 'ripples,' a family of sounds with drifting, sinusoidal, spectral envelopes—the complex spectro-temporal envelope of any broadband, dynamic sound can expressed as the linear sum of individual ripples. The collection of responses to all elementary ripples is the spectro-temporal transfer function. Previous experiments using ripples with downward drifting spectra suggested that the transfer function is separable, i.e., it is reducible into a product of purely temporal and purely spectral functions. Here we compare the responses to upward and downward drifting ripples, assuming separability within each direction, to determine if the total bi-directional transfer function is fully separable. In general, the combined transfer function for two directions is not symmetric, and hence units in AI are not, in general, fully separable. Consequently, many AI units have complex response properties such as sensitivity to direction of motion, though most inseparable units are not strongly directionally selective. We show that for most neurons the lack of full separability stems from differences between the upward and downward spectral cross-sections, not from the temporal cross-sections; this places strong constraints on the neural inputs of these AI units.

Keywords: *auditory cortex, spatial frequency, temporal frequency, separability, ripples*
Abbreviations: *AI = Primary Auditory Cortex, STRF = Spectro-Temporal Response Field, RF = Response Field, BF = Best Frequency, SVD = Singular Value Decomposition*
Running Title: *Spectro-Temporal Response Field Characterization by Dynamic Ripple Spectra*

Contents

1 Introduction

Only a few general organizational features are known in Primary Auditory Cortex (AI). They include a spatially ordered tonotopic axis (Reale and Imig 1980), bands of alternating binaural response properties (Middlebrooks et al. 1980), and

a variety of other response features that change systematically along the isofrequency planes such as thresholds (Schreiner et al. 1992), bandwidths (Schreiner and Sutter 1992), FM selectivity (Mendelson et al. 1993; Shamma et al. 1993), and asymmetry of response areas (Shamma et al. 1993). To derive a functionally coherent picture of these maps, it is necessary to integrate these features within a comprehensive descriptor of the unit responses, one that can be quantitatively derived and employed to predict responses to novel stimuli.

Traditionally measured *response areas* (RA) and iso-intensity response curves are inadequate because they rarely include response dynamics and cannot be used to predict responses quantitatively. An alternative is the Response Field (RF) (Schreiner and Calhoun 1995; Shamma et al. 1995), a static, purely spectral function analogous to the RA except for the use of broadband sounds (but see (Nelken et al. 1994) and (Sutter et al. 1996)). A dynamic generalization of the RF is the Spectro-Temporal Response Field (STRF), a characteristic function of a neuron obtained using broadband sounds (Aertsen and Johannesma 1981; Eggermont 1993 and references therein; Kvale and Schreiner 1995; Kowalski et al. 1996a; deCharms et al. 1998; Escabi and Schreiner 1999; Theunissen et al. 1999). A schematic of an idealized STRF is illustrated in Fig. 1. Qualitatively, its spectral axis reflects the range of frequencies that influence the response or firing rate of the neuron being characterized, and its temporal axis reflects how this influence changes as a function of time. Positive-valued regions of the STRF describe excitatory influence, and negative regions describe inhibitory influence. The interplay between the spectral and temporal axes can give multiple interpretations to the STRF, e.g., as a time evolving spectral response field, or a family of impulse responses labeled by frequency band.

Over the last few years, we have developed new methods to derive the STRFs and characterize the responses of both single and multiple units in the ferret Primary Auditory Cortex (AI) (Kowalski et al. 1996a; Kowalski et al. 1996b). These methods use “moving ripples”: time-varying, broadband sounds with sinusoidal spectral envelopes that drift at constant velocity along the logarithmic frequency axis. Fig. 2 illustrates the spectrogram of such a stimulus. Neuronal responses are vigorous and well phase-locked to these spectral and temporal envelope modulations, over a range of velocities and densities. Measuring the amplitude and phase of the locked component of the response enables one to construct *transfer functions*. A transfer function can be inverse-Fourier transformed to obtain the STRF that characterizes a unit’s dynamics and selectivity along the tonotopic axis.

In developing these measurement and analysis methods, we use two fundamental assumptions. The first is that the responses are substantially linear with

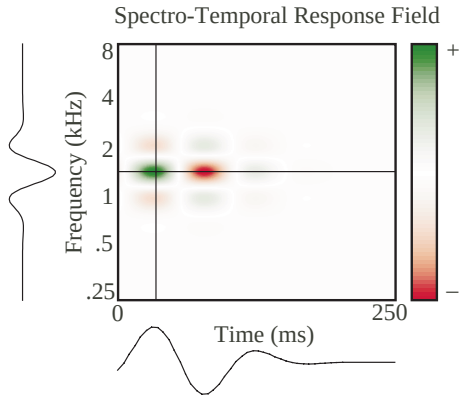

Figure 1: An idealized STRF, with spectral and temporal 1-dimensional sections.

respect to the time-varying spectral envelope of stimuli. In particular, this implies that the response to a spectro-temporally rich stimulus—whose envelope can always be described as the sum of multiple moving ripples—will be the sum of its responses to the individual ripple components. This assumption was confirmed by predicting successfully responses to the superposition of multiple ripples (Kowalski et al. 1996b). Further research on the origin and limits of this linear behavior, and the characterization of nonlinear aspects of the responses is needed.

The second important assumption deals with the separability of the temporal and spectral aspects of the responses. Specifically, we have demonstrated in other reports that temporal and spectral transfer functions can be measured independently of each other, and then combined with a simple product to compute the total transfer function (Kowalski et al. 1996a; Klein et al. 2000). The importance of this finding stems from its experimental implications for measuring the STRFs and theoretical consequences for the biophysical and functional models of the STRFs. On the experimental side, separability makes it possible to infer responses to all ripple velocities and peak densities based on only a pair of temporal and spectral transfer functions. Without this assumption, measuring the two dimensional transfer function is difficult because of the extended times needed to collect adequate spike counts. On the theoretical side, separability suggests that certain features of the STRF (as we shall discuss in detail below) are formed by independent (and likely sequential) spectral and temporal processing stages.

In our earlier study, separability was validated for ripples moving only in one direction (downwards in frequency), a notion also known as “quadrant separabil-

ity". In this report, we compare the separable functions (spectral and temporal) across upward and downward quadrants. If the functions are the same across quadrants, the responses are "fully separable" (i.e., they are separable); otherwise they are quadrant separable, which is a (specialized) form of inseparability.

Like quadrant separability, full separability has experimental and theoretical implications. On the experimental side, fully separable STRFs can be measured with either upward or downward moving ripples. Theoretically, fully-separable responses imply an STRF that is fully decomposable into the product of a purely temporal impulse response and a purely spectral response field. It also implies a unit that responds equally well to upward and downward moving ripples, and hence has necessarily a symmetric transfer function magnitude with respect to direction (Watson and Ahumada 1985). By contrast, cells that are only quadrant separable necessarily respond in asymmetric fashion with respect to direction, i.e., are direction-sensitive. Further theoretical aspects and biological implications of full separability and quadrant separability will be discussed in the second paper in this series (Simon et al. 1999a)

In the following sections, we first review the experimental methods and analysis procedures used. We then describe examples of the STRFs measured in AI and summarize the distribution of the STRF and transfer function parameters encountered. We focus on the issue of quadrant and full-separability, and propose measures to quantify them. Finally, we discuss the significance of the results and their relationship to results from similar auditory and analogous visual experimental paradigms. We shall restrict our presentation in this paper to measurements with singly presented moving ripples. In another paper (Klein et al. 2000), we have compared the results to STRFs measured with simultaneously presented ripples (Klein et al. 1999) and assess the linearity of the responses, assess how nonlinear factors affect the measurements, and directly confirm the property of quadrant separability.

2 Methods

2.1 Surgery and animal preparation

Data were collected from a total of 11 domestic ferrets (*Mustela putorius*) supplied by Marshall Farms (Rochester, NY). The ferrets were anesthetized with sodium pentobarbital (40 mg/kg) and maintained under deep anesthesia during the surgery. Once the recording session started, a combination of Ketamine (8

mg/Kg/Hr), Xylazine (1.6 mg/Kg/Hr), Atropine (10 μg/Kg/Hr) and Dexamethasone (40 μg/Kg/Hr) was given throughout the experiment by continuous intravenous infusion, together with Dextrose, 5% in Ringer solution, at a rate of 1 cc/Kg/Hr, to maintain metabolic stability. The ectosylvian gyrus, which includes the primary auditory cortex, was exposed by craniotomy and the dura was reflected. The contralateral ear canal was exposed and partly resected, and a cone-shaped speculum containing a miniature speaker (Sony MDR-E464) was sutured to the meatal stump. For more details on the surgery see (Shamma et al. 1993).

2.2 Recordings

Action potentials from single units were recorded using glass-insulated tungsten micro-electrodes with 5–7 MΩ tip impedances at 1 kHz. Neural signals were fed through a window discriminator and the time of spike occurrence relative to stimulus delivery was stored using a computer. In each animal, electrode penetrations were made orthogonal to the cortical surface. In each penetration, cells were typically isolated at depths of 350–600 μm corresponding to cortical layers III and IV(Shamma et al. 1993). In many instances, it was difficult to hold a single unit for extended recordings, and hence several units were recorded instead. Such data were labeled "multiunit recordings" and are explicitly designated as such and separated from the single unit records in all data presentations in the paper.

2.3 Acoustic stimuli

All stimuli are computer synthesized. For each unit isolated, initial tests are carried out using tonal stimuli to measure the basic frequency response curve at several intensities, to determine the Best Frequency (BF), the response area of the cell, and response thresholds. All other stimuli used in these experiments have broadband spectra with a sinusoidally modulated (or rippled) envelope

$$S(t,x) = L\left[1 + \Delta A \cdot \sin(2\pi \cdot w \cdot t + 2\pi \cdot \Omega \cdot x + \Phi)\right] \tag{1}$$

(or linear combinations of such envelopes), where $x = \log_2(f/f_0)$ is the number of octaves above the base frequency f_0. The ripple envelope resembles a drifting one-dimensional grating as illustrated in Fig. 2. Five independent parameters characterize the ripple envelope: (1) background level of the stimulus (L); (2) amplitude modulation of the ripple (ΔA) in % or dB; (3) ripple velocity (w) in units of cycles/s (or Hz); (4) ripple frequency (Ω) in units of cycles/octave; (5)

the initial phase of the ripple Φ. The spectra consist either of 20 or 100 tones per octave equally spaced along the logarithmic frequency axis, or with a spacing of 1 tone/Hz with an amplitude decay producing equal power per octave. The spectra typically span 5 octaves (e.g., 0.25–8 kHz or 0.5–16 kHz), with the range chosen such that the response area of the cell tested lay within the stimulus spectrum.

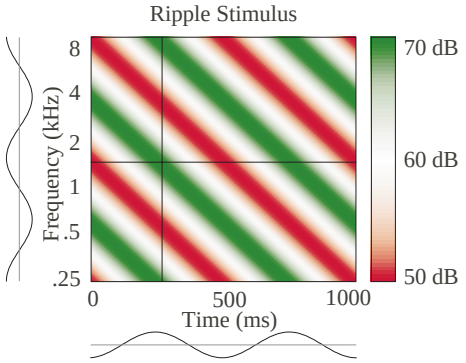

Figure 2: Envelope of a moving ripple, w = 2 Hz, Ω = 0.4 cycles/octave, $\Phi = -90°$, with a 10 dB amplitude modulation around a 60 dB base, with spectral and temporal 1-dimensional sections. Ripple phase changes linearly with time and spectral position (in octaves).

A single-ripple stimulus at overall level L dB SPL would typically be composed of 101 logarithmically spaced components, each at $L - 10\log_{10}(101) \approx L-$ 20 dB . The overall stimulus level was chosen on the basis of threshold at BF; typically L was set 10–20 dB above threshold. High levels ($L \geq 70$ dB) were avoided to ensure the linearity of our stimulus delivery system. The amplitude of a single ripple was defined as the maximum percentage or logarithm change in the component amplitudes. Ripple amplitudes were either at 90% or at 10 dB modulation, except for a few recordings in which we studied the effect of depth modulation on responses.

The ripple velocities w and ripple densities Ω used were determined by the response properties of the neuron, but the typical range used was $|w| < 25$ Hz (with some units requiring up to 100 Hz) and $|\Omega| < 1.6$ cycles/octave (with some units requiring up to 4 cycles/octave). Single ripples were always presented with $\Phi = 0$. By the convention established in Eq. 1, a ripple whose timbre is always moving downward in frequency, as in Fig. 2, has positive w and positive Ω. A ripple whose spectral peaks are always moving upward in frequency has negative w and positive Ω. Also by Eq. 1 and using the trigonometric identity $\sin(\alpha) = \sin(-\alpha + \pi)$,

a ripple with ripple velocity w, ripple frequency Ω, and phase constant Φ is identical to the ripple with ripple velocity $-w$, ripple frequency $-\Omega$, and phase constant $-\Phi + \pi$, so we may constrain $\Omega \geq 0$ without loss of generality.

The stimulus bursts had an 8 ms rise-fall time and duration of 1 s or 1.7 s, repeated every 3-4 seconds. All stimuli were gated and fed through an equalizer into the earphone. Calibration of the sound delivery system (to obtain a flat frequency response up to 20 kHz) was performed in situ with the use of a 1/8-in. Brüel & Kjaer 4170 probe microphone. The microphone was inserted into the ear canal through the wall of the speculum to within 5 mm of the tympanic membrane. The speculum and microphone setup resembles closely that suggested by Evans (Evans 1979).

2.4 Theoretical considerations

2.4.1 Defining the STRF

The fundamental goal of this work is to measure STRFs in AI. The STRF is defined here as a spectro-temporal function $STRF(t, x)$. The linear response rate $y(t)$ of a cell is then related to its $STRF(t, x)$ and the spectro-temporal envelope of the stimulus $S(t, x)$ by $y(t) = \int\int dt'\, dx S(t' - t, x) \cdot STRF(t, x)$, i.e., convolution along the time dimension t and integration along the spectral dimension x.

We measure the STRF through measurement of its two-dimensional Fourier transform, or transfer function $T(w, \Omega) = \mathcal{F}_{w\Omega}\left[STRF(t, -x)\right]$, and then inverse transform to compute the STRF, where the coordinates dual to t and x are w and Ω respectively (see Fig. 3). By measuring the sinusoidal component with frequency w of the response $y_{w\Omega}(t)$ of a cell to a ripple of specific ripple velocity w and ripple density Ω, we can obtain the transfer function $T(w, \Omega)$ at one point in w–Ω space (Depireux et al. 1998):

$$\begin{aligned} y_{w\Omega}(t) &= \iint dt' dx'\, STRF(x', t')\ \sin 2\pi[w(t - t') + \Omega x'] \\ &= |T(w, \Omega)|\ \sin\left[2\pi w t + \Phi(w, \Omega)\right]\ . \end{aligned} \tag{2}$$

This way, we derive the amplitude $|T(w, \Omega)|$ and phase $\Phi(w, \Omega)$ of the complex transfer function $T(w, \Omega)$ by measuring the amplitude and phase of the (real) response of the cell. Note that the use of complex numbers in the derivation of Eq. 2 and equations below is not theoretically necessary, but it does simplify the

calculations in the transfer function space considerably. By the definition of the transfer function, it follows that the inverse Fourier transform of $T(w, \Omega)$ is the STRF of the cell:

$$STRF(t, x) = \mathcal{F}^{-1}{}_{t,-x}\left[T_{w\Omega}\right] \tag{3}$$

Because $STRF(t, x)$ is real, but $T(w, \Omega)$ is complex, there is complex conjugate symmetry,

$$T(-w, -\Omega) = T^*(w, \Omega) \tag{4}$$

which also holds for the Fourier transform of any real function of t and x.

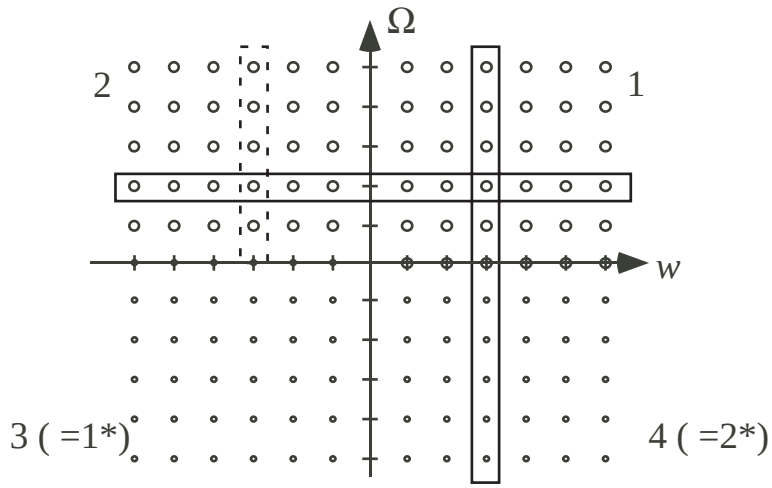

Figure 3: To measure the complete ripple transfer function of an arbitrary STRF we would need to measure the response of the cell to all the ripples represented by large circles above. The smallest circles correspond to redundant ripples by complex conjugation. The value of the transfer function along the $w = 0$ axis is set to zero, because the modulation transfer function is not well-defined there. Quadrant separability allows us to measure only the responses to ripples enclosed by the solid boxes. The transfer function in the dashed box is equal to the transfer function in the bottom half of the vertical box but with the opposite phase.

2.4.2 Defining and assessing separability

Separability is an important property of the transfer functions as discussed earlier. A fully separable transfer function is one that factorizes into a function of w and a function of Ω over all quadrants: $T(w, \Omega) = F(w) \cdot G(\Omega)$. This implies that

$STRF(t,x)$ is spectrum-time separable: $STRF(t,x) = IR(t) \cdot RF(x)$. In this case, we only need to measure the transfer function for all Ω at a convenient w, and for all w at a convenient Ω. $F(w)$ and $G(\Omega)$ are each complex-conjugate symmetric ($F(-w) = F^*(w)$, $G(-\Omega) = G^*(\Omega)$) because $IR(t)$ and $RF(x)$ are real, so we need only consider the positive values of each. This dramatically decreases the number of measurements needed to characterize the STRF.

A transfer function may also be only partially separable, in that it is separable only for ripples moving in a given direction. In this case, the transfer function is called quadrant separable, and can be expressed as the product of two independent functions:

$$T(w,\Omega) = \begin{cases} F_1(w)\, G_1(\Omega) & w > 0, \Omega > 0 \\ F_2(w)\, G_2(\Omega) & w < 0, \Omega > 0 \end{cases} \tag{5}$$

where the subscript 1 indicates the $w > 0, \Omega > 0$ quadrant, and the subscript 2 the $w < 0, \Omega > 0$ quadrant (see Fig. 3). Note that by reality of the STRF, the value of the transfer function in quadrants 3 ($w < 0, \Omega < 0$) and 4 ($w > 0, \Omega < 0$) is complex conjugate to the value in quadrants 1 and 2 respectively. In this case, the STRF is not separable in spectrum and time, but is the linear superposition of two functions, one with support only in quadrant 1 (and 3), and one with support only in quadrant 2 (and 4).

Full and quadrant separability need not be an all-or-none property, but rather can be assessed in a graded fashion. To do so, we employ singular value decomposition (SVD) methods to compute the *singular matrix* (Λ) corresponding to the transfer function matrix $T(w,\Omega)$ as:

$$T = U \cdot \Lambda \cdot V^\dagger, \qquad \Lambda = diag(\lambda_1, \lambda_2, \ldots, \lambda_n), \quad \lambda_1 \geq \lambda_2 \geq \ldots, \tag{6}$$

where $U, V^\dagger$ are the corresponding matrices of singular vectors (Haykin 1988). Because of the presence of noise in the measurement, all λs are expected to be non-zero, with their value decreasing asymptotically to a value below the noise floor. With respect to this floor, the number of significant singular values in Λ varies depending on the nature of the transfer function T:

> **Fully separable**: If Λ has *only one* significant singular value then the matrix T is fully separable, i.e., expressible as the product of two vectors — a purely temporal and a purely spectral function. These functions will be the first singular vectors in U and $V^\dagger$.

Totally inseparable: If Λ has *more than two* relatively sizeable singular values, then the matrix T is totally inseparable. The degree of inseparability can be indicated by the ratio $\lambda_1^2 / \sum_i \lambda_i^2$.

Quadrant separable: If Λ has *exactly two* significant singular values then the matrix T is inseparable but possibly quadrant separable. To check, we apply SVD to each quadrant separately. Just as above, if only one eigenvalue λ is large, then the transfer function in that quadrant is separable, otherwise it is not.

In this report, our experiments assume quadrant separability since we measure in each quadrant a temporal transfer function at only one Ω and a spectral transfer function at only one w. Our goal is to test for full separability as in the steps above. We shall also be interested in examining the origin of inseparability. Specifically, we shall compute three factors that give rise to inseparability:

- The relative power in the first and second quadrants:

$$\alpha_d = \frac{P_2 - P_1}{P_1 + P_2}, \tag{7}$$

  where $P_1 =$ (power in quadrant 1)$= \lambda_1^2$, and $P_2 =$ (power in quadrant 2) $= \lambda_2^2$. Absolute value of α_d near one implies strong preference of the responses to the direction of ripple movement, and hence strong inseparability.

- The asymmetry of the spectral transfer function around $\Omega = 0$ is

$$\alpha_s = 1 - \left| \frac{\sum_{\Omega>0} G_1(\Omega) \cdot G_2^*(\Omega)}{\sqrt{\sum_{\Omega>0} |G_1(\Omega)|^2 \cdot \sum_{\Omega>0} |G_2(\Omega)|^2}} \right|, \tag{8}$$

  where the quantity inside the absolute value bars is the (complex) correlation between $G_1(\Omega)$ and $G_2(\Omega)$. Index α_s values near zero imply strong asymmetry (i.e., lack of correlation) in the transfer function to different directions, and hence strong inseparability.

- The asymmetry of the temporal transfer function around $w = 0$ is

$$\alpha_t = 1 - \left| \frac{\sum_{w>0} F_1(w) \cdot F_2(-w)}{\sqrt{\sum_{w>0} |F_1(w)|^2 \cdot \sum_{w>0} |F_2(-w)|^2}} \right|, \tag{9}$$

where the quantity inside the absolute value bars is the (complex) correlation between $F_1(w)$ and $F_2^*(-w)$. Index α_t values near zero imply strong asymmetry (i.e., lack of correlation) in the transfer function to different directions, and hence strong inseparability.

2.4.3 Effects of non-linearity

The most prominent non-linear distortions are approximate half-wave rectification and compression. The half-wave rectification is primarily due to the positivity of spike rates (ordinarily the steady-state response to a flat spectrum is significantly less than half the peak firing rate of the unit); the distortion of a sinusoid due to half-wave rectification does not affect the phase of the response, and its effect on the amplitude of the first Fourier component is a constant factor (independent of w and Ω). The distortion due to compression or saturation, similarly, does not affect the phase of the Fourier transform components of the response, and similarly affects the amplitude only by an overall constant factor, for stimuli of moderate level.

2.5 Data reduction

Many of the data analysis methods described here are similar or straightforward extensions of those developed earlier in (Kowalski et al. 1996a) and those will be only briefly reviewed here. Figs. 4 and 5 illustrate the nature of the responses to the ripple stimuli and the analysis to extract the spectral (Fig. 4) and temporal (Fig. 5) transfer functions. In Fig. 4A, the ripples are presented at 8 Hz, for ripple densities from -1.6 cyc/oct to 1.6 cyc/oct in steps of 0.2 cyc/oct. Each stimulus is presented 15 times. The ripple begins to move and the sound is acoustically turned on at t = 0 ms with a linear ramp over 8 ms. For each ripple density, we compute a 16-bin period histogram based on the responses starting at 120 ms (to exclude the onset response). A 16-point FFT is then performed on the period histogram, and the amplitude and phase of the first component is taken to be the amplitude and phase of the transfer function. If the modulation of the response were that of a purely linear system, the higher FFT coefficients would be negligible, but because of half-wave rectification and other non-linearities, they usually are significant. Analogous steps are followed in measuring the temporal transfer function as shown in Fig. 5 where ripples are presented at 0.4 cyc/oct, for ripple velocities from -24 Hz to 24 Hz in steps of 4 Hz.

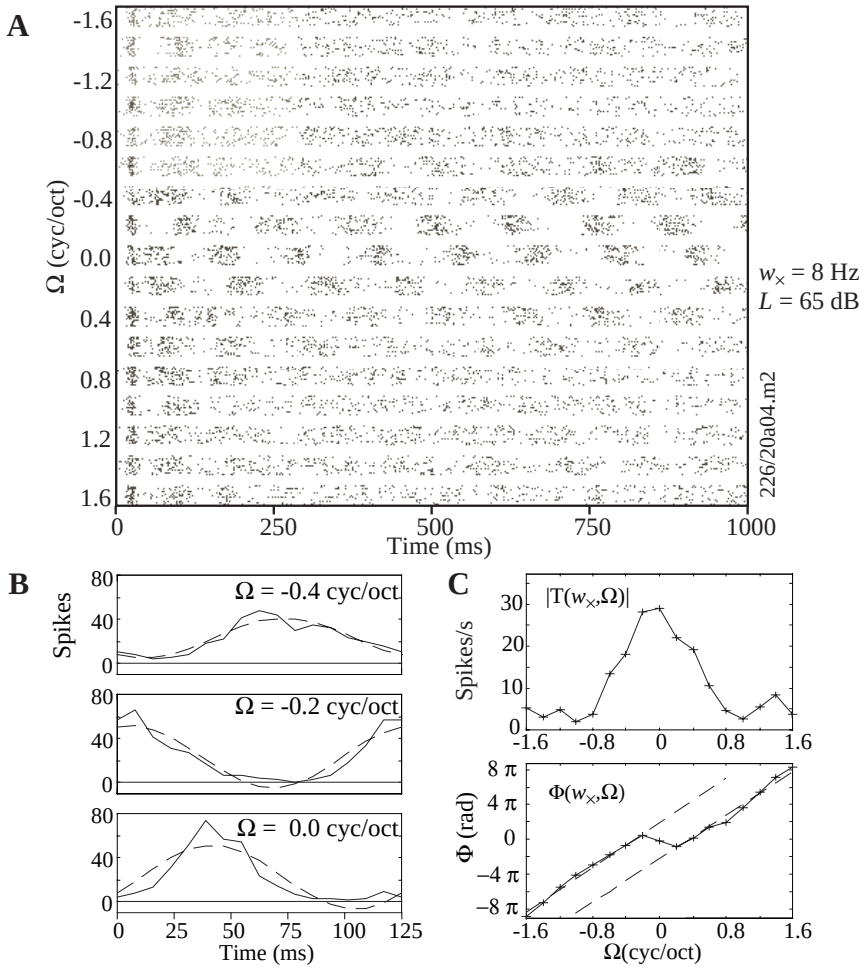

Figure 4: Data analysis for ripples of fixed ripple velocity and varying ripple frequencies. **A**: Raster plot of responses. Each point represents an action potential, and each ripple stimulus is presented 15 times. **B**: Period histogram for 3 example ripple frequencies, with their sinusoidal fits. Note how the position of the peak of the best fit changes linearly with ripple frequency; this can also be seen by the banding pattern in **A**. **C**: Magnitude and phase of the period histogram fits. With the phase convention used for these stimuli, ripples with $\Omega < 0$ (quadrant 4) are equivalent to ripples with $w < 0$ (quadrant 2), using the conversion $(w, \Omega, \Phi) \rightarrow (-w, -\Omega, -\Phi + \pi)$.

In order to construct the two dimensional spectro-temporal transfer function, we assume quadrant separability, measure the transfer function along the cross-sections shown in Fig. 3, to combine these spectral and temporal cross sections as

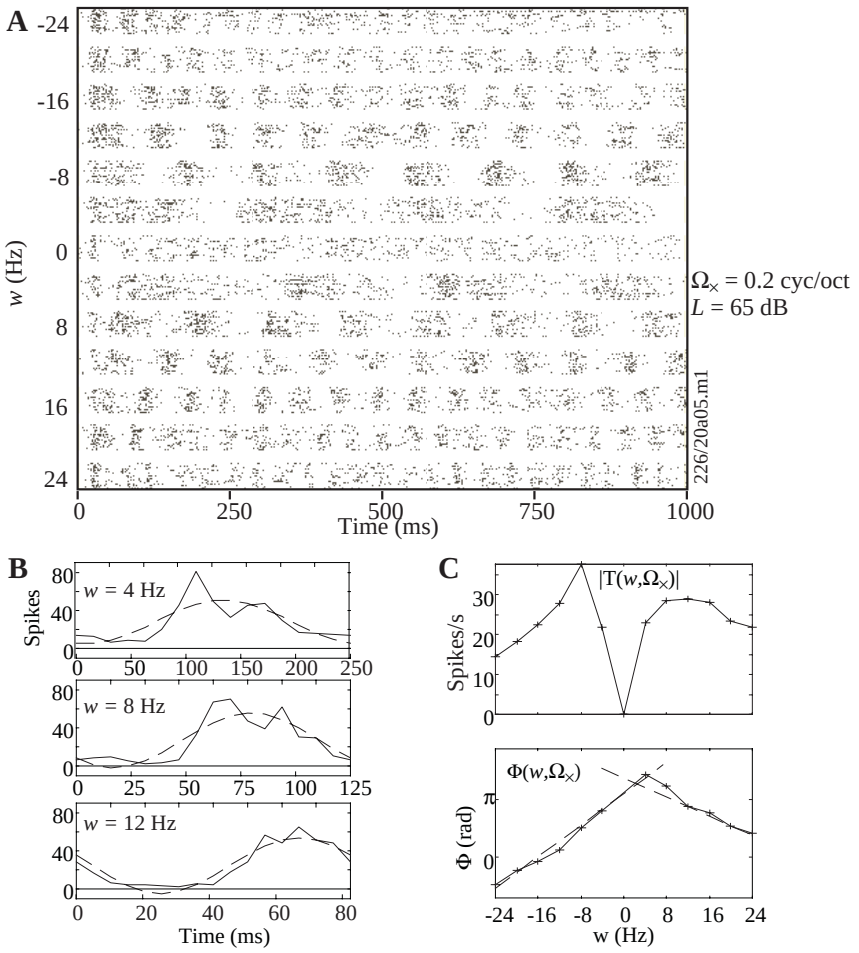

Figure 5: Data analysis from ripples of fixed ripple frequency and varying ripple velocities. **A:** Raster plot of responses. Each point represents an action potential, and each ripple stimulus is presented 15 times. **B:** Period histogram for 3 example ripple velocities. Note how the position of the peak of the best fit changes linearly with ripple velocity. **C:** Magnitude and phase of the period histogram fits.

illustrated in Fig. 6. For each quadrant, the transfer function is the outer product of the cross-section, divided by the (complex) value of the transfer function at the crossover ($\times$) point (in Fig. 6 the point is $(w_{\times 1}, \Omega_{\times 1}$ = (8 Hz, 0.4 cycles/octave) in quadrant 1 and $(w_{\times 2}, \Omega_{\times 2}$ = (-8 Hz, 0.4 cycles/octave) in quadrant 2).

$$T(w,\Omega) = T(w_{\times q},\Omega) \cdot T(w,\Omega_{\times q}) \,/\, T(w_{\times q},\Omega_{\times q}) \tag{10}$$

where $q = 1, 2$ are the independent quadrants 1 and 2. In practice, the value of the transfer function along the two cross-sections was measured at two different times, giving two measurements of the transfer function at each crossover point $T(w_{\times q}, \Omega_{\times q})$. The results of the two measurements may differ, and so we use the (complex) geometric mean of the two measured values as the divisor in Eq. 10, $T_{\mathit{eff}}(w_{\times q}, \Omega_{\times q}) = [T_{1^{st}}(w_{\times q}, \Omega_{\times q}) T_{2^{nd}}(w_{\times q}, \Omega_{\times q})]^{1/2}$.

The ratio $T_{1^{st}}(w_{\times q}, \Omega_{\times q}) / T_{2^{nd}}(w_{\times q}, \Omega_{\times q})$, which should be unity, reflects the noise in the system, and is used to estimate reliability below.

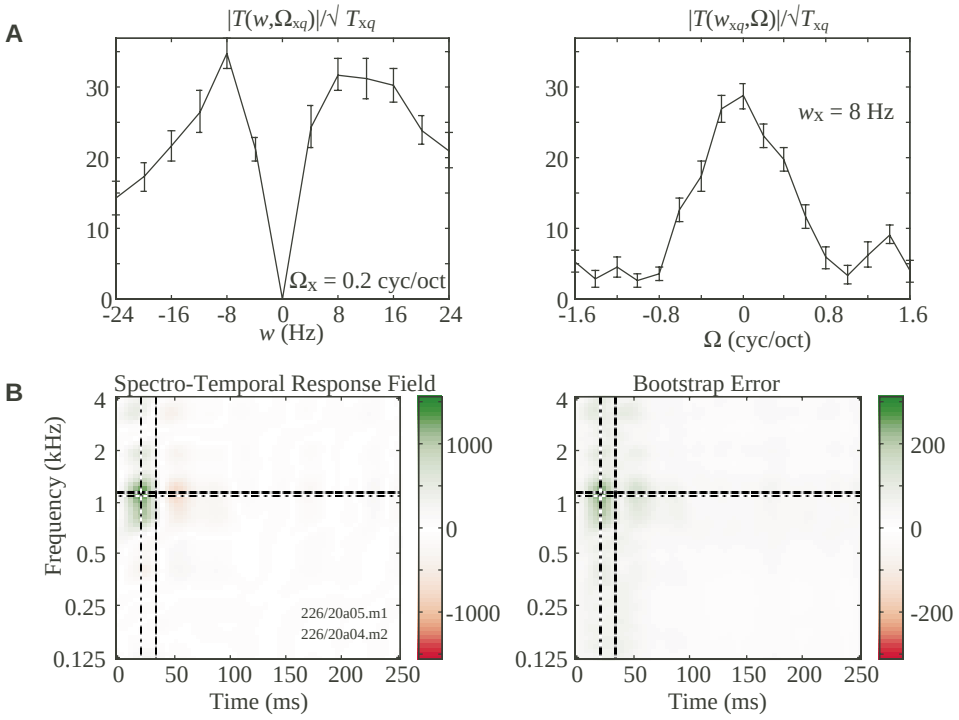

Figure 6: Deriving the spectro-temporal transfer function, STRF, and related parameters. **A**: Magnitude of the temporal (left) and spectral (right) transfer function cross-sections, normalized by the values at the cross-over points (Eq. 10). The error bars are computed by the bootstrap method, explained below. **B**: The STRF of the cell computed by an inverse Fourier transform of the complex transfer functions. To the right is the error estimate of the STRF, using the same scale multiplied by a factor of 5, resulting in error parameters of $\delta = 0.03$ and $\epsilon = 0.06$. See Table 1 for details.

The value of the transfer function along the $w = 0$ axis is set to zero, because the modulation transfer function is not well-defined there. The value of the trans-

fer function along the $\Omega = 0$ axis is not measured directly, so the value used is the mean of the value inferred from being the boundary of quadrant 1 and that inferred from being the boundary of quadrant 2.

Once the values of transfer function for quadrants 1 & 2 and their boundaries are measured, the values for quadrants 3 & 4 are given by Eq. 4 (see also Fig. 3). The STRF is then computed by an inverse Fourier transform (as in Eq. 3) and is illustrated in Fig. 6B (left panel). This interpolated version of the STRF (used in most figures in this paper) is obtained by using Eq. 3 on a the transfer function padded with zeros at high $|w|$ and $|\Omega|$, where the transfer function vanishes (see Fig. 6A).

2.6 Deriving STRF parameters from the phase functions

Numerous parameters can be derived from the STRF (or equivalently the transfer function) that are analogous to traditional response measures such as BF, tuning curve bandwidth, and latency. Most of these parameters are best derived from analysis of the phase of the transfer functions.

We model the phase of the transfer function within each quadrant $\Phi^q(w, \Omega)$, $q = 1, 2$ (see Eq. 2) as a linear function of w and Ω :

$$\Phi^q(\Omega, w) = -2\pi w \tau_d^q + 2\pi \Omega x_m^q + \chi^q, \tag{11}$$

where τ_d^q is the mean or group delay of the STRF (a portion of which comes from the response latency), $x_m^q = \log_2 (f_m^q / f_0)$ is the mean frequency in octaves around which the STRF is centered (putting it near the BF), and χ^q is a constant phase angle, for each quadrant q. The complex-conjugate symmetry of the transfer function means that these six independent parameters describe the phase everywhere in the w–Ω plane. The convention of the minus sign before τ_d allows the time-dependent responses to be functions of $(t - \tau_d)$, as is appropriate for a delay.

The justification for assuming linear fits of the phase functions has been discussed in detail earlier in (Depireux et al. 1998), and is strongly motivated by the data (Kowalski et al. 1996a). Note, however, that the assumption of *phase* linearity is used only for parameter estimation and is not assumed in computing the STRF. The first linear term in Eq. 11 stems from the fact that auditory units differing in their mean neural delays will exhibit linear phase dependence on w with different slopes depending on the delay. Analogous arguments apply for units that are located at different places along the tonotopic axis: the response phase of different units (with otherwise identical STRFs) should change linearly with Ω at

different rates, depending on the relative center frequency location. In both cases, the slopes of the linear phase function indicate the absolute shift of the STRF relative to the origin, i.e. the mean time delay τ_d^q relative to the start of the stimulus, and the center frequency x_m^q relative to the low frequency edge of the ripple spectrum. The linear phase model does not assume that the linear phase shifts, τ_d^q and x_m^q, are equal across quadrants, but biology suggests that $f_m^1 \approx f_m^2$ from tonotopy and $\tau_d^1 \approx \tau_d^2$ since the temporal delays of the neural inputs are not segregated by quadrant. This is shown experimentally below.

An interpretation of τ_d, for each quadrant, is that it is the sum of the pure response latency and (roughly) half the temporal width of the STRF. This is in contrast to the STRF's peak delay, τ_{STRF}, defined to be the delay for which the STRF achieves its maximum value, which may lead or lag τ_d depending on the constant temporal phase shift, θ, defined below. Similarly, f_m, for each quadrant, may or may not fall on the STRF's best frequency, BF_{STRF}, defined to be the frequency at which the STRF achieves its maximum value, depending on the constant spectral phase shift, ϕ, defined below.

A convenient convention for interpreting the constant component of the phase is to break up the constant phase angle χ^q into two parts:

$$\chi^1 = -\theta + \phi,\ \chi^2 = \theta + \phi. \tag{12}$$

θ and ϕ are, respectively, the temporal polarity and spectral asymmetry of the STRF. Spectral asymmetry parametrizes the balance of the STRF along the spectral axis about its center. For example, a unit with $\phi = 0$ would have its BF_{STRF} in the center of the spectral envelope of the STRF, possibly surrounded by inhibitory regions. A unit with $\phi > 0$ would have its BF_{STRF} at a lower frequency than the center of the STRF, with an inhibitory sideband above BF_{STRF}. A unit with $\phi < 0^\circ$ would have its BF_{STRF} at a higher frequency than the center of the STRF, with an inhibitory sideband below BF_{STRF} (see example in Fig.4C of Shamma et al. 1995). Similarly the temporal polarity parametrizes the balance of the STRF along the temporal axis about its center: whether the peak response occurs before or after regions of inhibition, respectively $\theta < 0$ ("onset response at BF") or $\theta < 0$ ("offset response at BF"). There is an ambiguity in fixing θ and ϕ which we remove by restricting ϕ to lie between -90° and +90°, while θ ranges the full -180° to +180°. See Fig. 7 as an illustration of the phase behavior in the different quadrants.

In past reports (Kowalski et al. 1996a), θ and ϕ could be measured without measuring the transfer function in the upward moving quadrant 2 by measuring

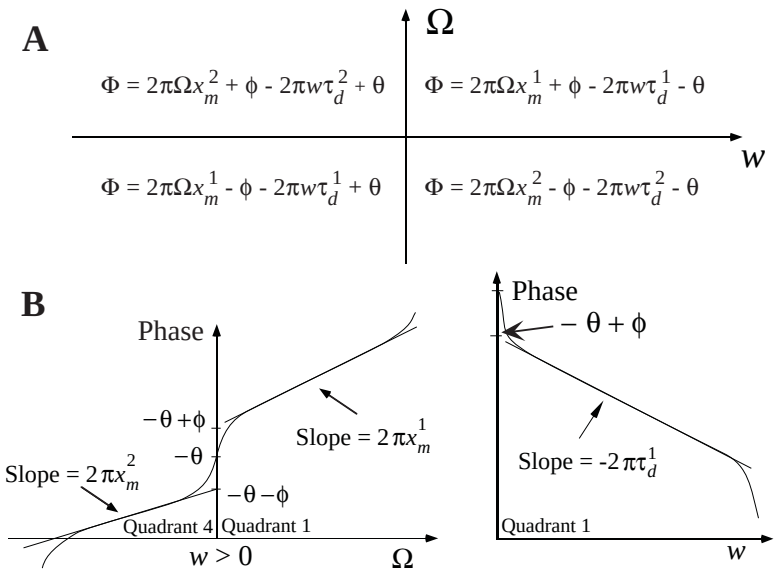

Figure 7: **A**: The phase of the transfer function can be described by a linear fit containing 6 parameters over most of the relevant regions of the w–Ω plane. **B**: In this cartoon the slope is constant for most of the curves, after (left) $-2\pi w\tau_d^q$ has been removed from the corresponding quadrants, corresponding to a center frequency that is independent of the ripple frequency, and (right) after $2\pi\Omega x_m^1$ has been removed, corresponding to a delay that is independent of ripple velocity. At very small ripple frequencies (long ripple periodicity), center frequency is less meaningful, and similarly for small ripple velocity and delay, respectively. At large ripple velocity the slope asymptotes to the signal-front delay, but when this occurs the small amplitude of the transfer function makes it difficult to measure the phase. See Dong and Atick (1995) and Papoulis (1962).

the constant component of the phase in quadrant 1 ($\chi^1 = -\theta+\phi$) and along the w-axis, where the constant component of the phase is expected to be the mean across the quadrants ($(\chi^1 - \chi^2)/2 = -\theta$) (note the change in convention of $\theta \rightarrow -\theta$ between the present work and Kowalski et al. 1996a).

Because of response variability, we only fit to those points of the transfer function that have more than half of the response power in the first component of the Fourier transform. Then the fit is done across the entire two dimensional phase plane, for each quadrant. Ultimately, our unwrapping method is less than ideal, and estimates of θ and ϕ especially reflect that (Ghiglia and Pritt 1998).

2.7 Estimating response variability: the bootstrap method

Variability in our experiments originates from multiple sources, including internal neural mechanisms (e.g., Poisson-like distributions of spike times), extracellular recording/identifying methods, and equipment noise. Quantitative estimates of the reliability of our measurements is crucial to its analysis and subsequent interpretation. A method of variability estimation that is especially appropriate to these measurements is the bootstrap method (Efron and Tibshirani 1993; Politis 1998).

The essence of this method is to use "resamples", in which N samples of bootstrap data are drawn *with replacement* from the N original samples of data. Repeating this procedure a large number of times creates a population of bootstrap resamples whose probability distribution is a good estimator of the probability distribution from which the original data was drawn.

To illustrate this procedure, consider measuring the transfer function at a point (w, Ω). This is done by presenting the same (w, Ω) stimulus N times and constructing a period histogram based on all N sweeps. The amplitude and phase of the first Fourier component of the period histogram are assigned to the amplitude and phase of the transfer function. A single bootstrap resampling of the responses will have N sweeps, where, because they are drawn from the original responses with replacement, some will be duplicated and some will be unused. Nevertheless, a period histogram is constructed, and the bootstrap estimate of the transfer function is assigned to its first Fourier component. Performing a large number of bootstrap resamples results in a population of estimates for the transfer function. This population has a mean, variance, and higher order moments. These moments are estimators of the moments of the original population (of all transfer functions of all allowable neuronal responses to the stimulus). For example, the standard deviation of all bootstrap estimates of the transfer function is an estimator of the standard deviation all measurements of the transfer function. This allows us to put error bars on our transfer functions and STRFs.

2.8 Effects of crossover point errors

Another significant source of error is the difference between the responses of repeated measurements at the transfer function crossover points. The ratio of these independent measurements, $T_{1^{st}}(w_{\times}^{q}, \Omega_{\times}^{q})/T_{2^{nd}}((w_{\times}^{q}, \Omega_{\times}^{q})$ should be unity. When not unity, it reflects the same variability measured by the bootstrap method, but also additional systematic error from having measured the two transfer function

cross-sections at different times. To account for this disparity, the total squared error of the STRF is set to the sum of the bootstrap STRF variance and the square of the crossover error $\sigma_\times$,

$$\sigma^2_{STRF} = \sigma^2_{Bootstrap} + \sigma^2_\times \tag{13}$$

where $\sigma_\times(t,x)$ captures the systematic error from not having taken all data at the same time, and is given by:

$$\sigma_\times(t,x) = \left(\max_q \left(\frac{\max\left(\left|T_1^q(w_\times^q,\Omega_\times^q)\right|, \left|T_2^q(w_\times^q,\Omega_\times^q)\right|\right)}{\left|T_{\mathit{eff}}^q\left(w_\times^q,\Omega_\times^q\right)\right|} \right) - 1 \right) * \left|STRF\left(t,x\right)\right| \tag{14}$$

Finally, we collapse the error over the entire (t,x) plane into two dimension-less terms δ and ϵ.

$$\delta = \frac{1}{\Delta T \Delta X} \iint dt\, dx\, \sigma_{STRF}\left(t,x\right) \frac{1}{\max\left(\left|STRF(t,x)\right|\right)} \tag{15}$$

$$\epsilon = \iint dt\, dx\ \left[\sigma_{STRF}\left(t,x\right)\right]^2 \Big/ \iint dt\, dx\ \left[STRF\left(t,x\right)\right]^2 \tag{16}$$

where ΔT and ΔX are the length of time and number of octaves over which the STRF was measured.

3 Results

Data presented here were collected from 22 single unit and 54 multiunits recordings in 11 ferrets. In the summary histograms, both single units and multiunits are included but are distinguished from each other.

Most units encountered in AI respond well to moving ripples. Responses are typically phase-locked to the moving envelope of the ripple over a range of ripple velocities and densities. However, out of a total of 172 recordings made, only 76 cases provided adequate quality and quantity of responses. The reasons for this low yield vary. For example, we have encountered responses from a few units that were either poorly phase-locked, or were inconsistent from trial-to-trial; such units were abandoned since our analysis methods are unsuitable for their characterization. Also, because of extended recording times (typically about an hour), units were sometimes lost before sufficient data could be collected to carry

out a full analysis. In other cases, the unit or animal changed state during the recording session, rendering the data unreliable. To eliminate such data, we use units only with values of $\delta \leq 0.12$ and $\epsilon \leq 0.7$ (see *Methods*) as the threshold for rejecting the data. These reliability statistics takes into account most of the above sources of error.

STRF	f_m^1 (kHz)	f_m^2 (kHz)	τ_d^1 (ms)	τ_d^2 (ms)	ϕ_m (deg)	θ (deg)	δ %	ϵ %	sngl/ mult
Fig 6	1.1	1.1	21	34	-24	-46	3	6	mult
Fig 8 A	1.5	1.9	25	23	4	- 69	3	14	mult
Fig 8 B	1.4	1.6	32	23	-43	- 58	8	29	mult
Fig 8 C	1.1	2.0	20	35	-21	-105	5	25	mult
Fig 9 A	3.8	4.5	29	29	-36	-110	3	4	mult
Fig 9 B	1.5	1.8	21	20	7	- 57	2	8	mult
Fig 9 C	3.9	4.6	13	5	-68	- 67	3	36	sngl
Fig 10 A	0.56	0.68	21	12	-26	-63	2	6	sngl
Fig 10 B	0.49	0.57	25	14	40	-35	9	24	mult
Fig 10 C	1.2	1.14	47	43	4	140	4	11	mult

Table 1: Characteristic parameters of STRFs shown

3.1 Responses to moving ripples

On average, AI units synchronize their responses to upward and downward moving ripples equally effectively, with ripple velocities ranging from 2 to over 100 Hz, and ripple densities up to 4 cyc/oct. Examples of three temporal and spectral transfer function magnitudes are shown in Fig. 8, each with its corresponding STRF. In all cases, units respond well only over a specific range of ripple velocities and ripple densities, but the detailed shape and extent of the transfer functions vary from one unit to another. For instance, the unit in Fig. 9A responds well only to ripple velocities of $\pm$4 Hz, whereas the unit in Fig. 9C responds well at least up to $\pm$64 Hz. The unit in Fig. 6 responds well to ripple densities within $\pm$0.4 cyc/oct, whereas the unit in Fig. 10A responds over a wider range of densities ($\pm$0.8), but poorly at 0 cyc/oct.

Units also vary significantly in the asymmetry of their transfer functions with respect to the direction of the moving ripple. For example, responses to the two

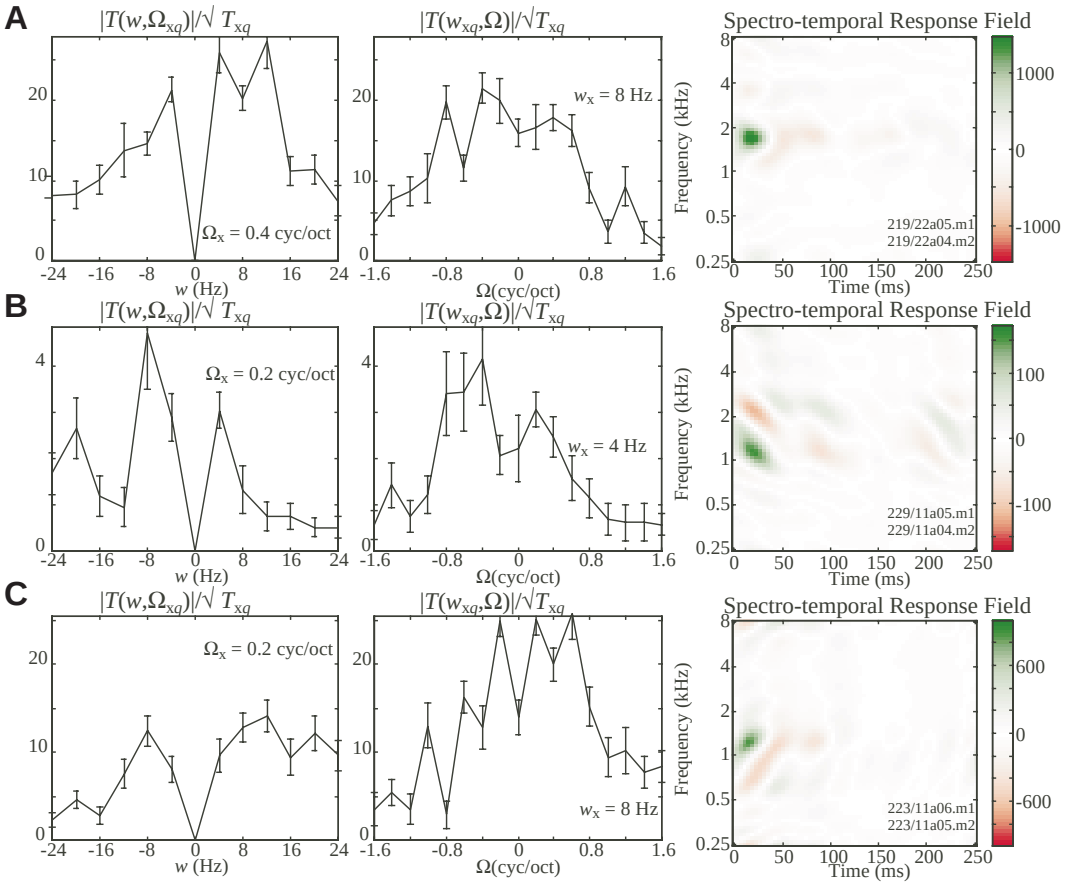

Figure 8: Three examples of Spectro-temporal transfer function sections, corresponding STRFs. For each row (**A,B,C**): (left and middle): magnitude of the temporal (left) and spectral (middle) transfer functions. All other details are as in Fig. 6; (right). STRFs

directions are relatively equal (transfer functions are roughly symmetric) in Figs. 6 and 9A. By comparison, the transfer functions in Fig. 8A–C are asymmetric. Unit 8B responds better to upward moving ripples; unit 8C responds over a wider range to downward moving ripples. These asymmetries are discussed in depth later in the context of transfer function separability.

The STRFs derived from these transfer functions commonly exhibit alternating regions of positive peaks and negative basins, interpreted here as excitatory and inhibitory regions, respectively. The four STRFs illustrated in Figs. 6 and 8 are of units that are tuned between 1 and 2 kHz. However, the shapes of the

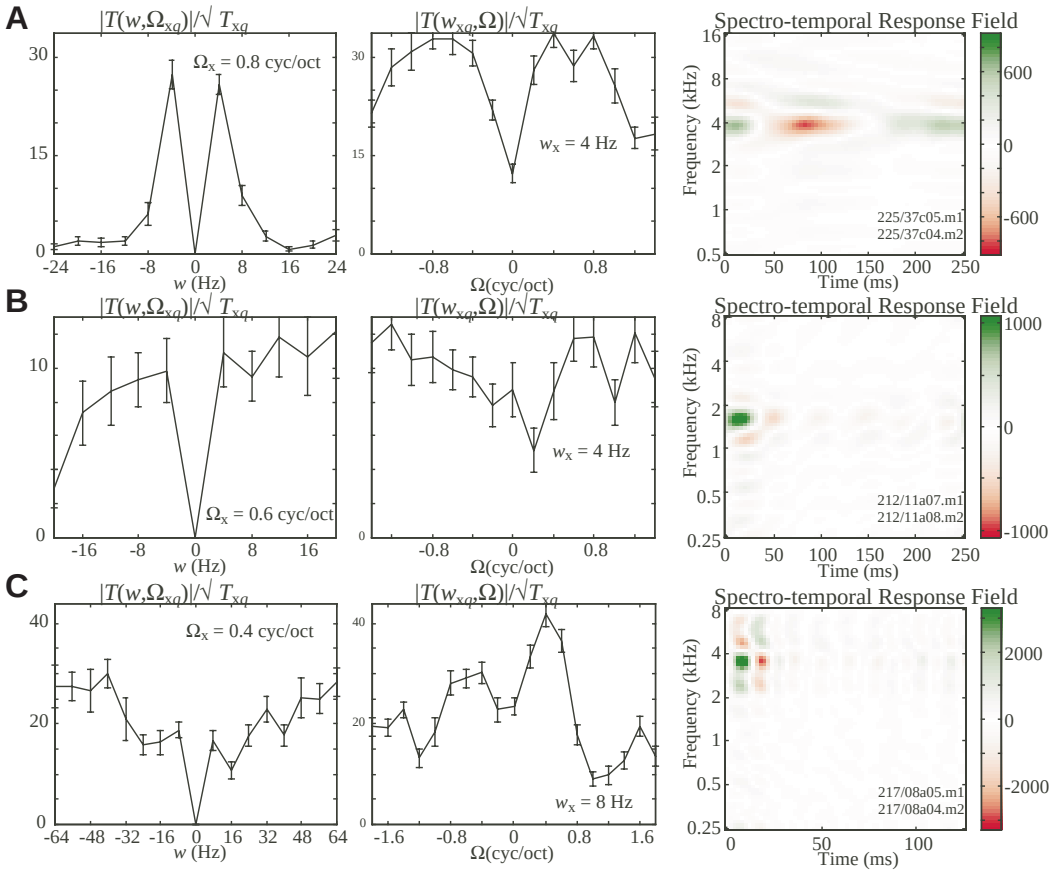

Figure 9: Further examples of Spectro-temporal transfer function sections, corresponding STRFs. Conventions as in Fig. 8. **A**: with narrow ripple velocity bandwidth, **B**: with broad ripple velocity bandwidth, **C**: a spectrally asymmetric unit.

surrounding inhibitory regions vary considerably reflecting the different temporal and spectral transfer functions. For instance, STRFs maybe relatively symmetric (Fig. 8A) or asymmetric (Fig. 9C). They can be clearly directional, i.e., tilted upwards (Fig. 8B) or downwards (Fig. 8C) on the spectro-temporal surface.

As is evident, STRFs display a wide variety of shapes that are briefly described below. For example, the majority of AI cells exhibit STRFs with a simple excitatory field and varying amounts of inhibitory surround. The first peak of the excitatory portion indicates the BF of the unit, while its extent reflects its tuning curve (or iso-intensity response curve). The center of the whole STRF (i.e., in-

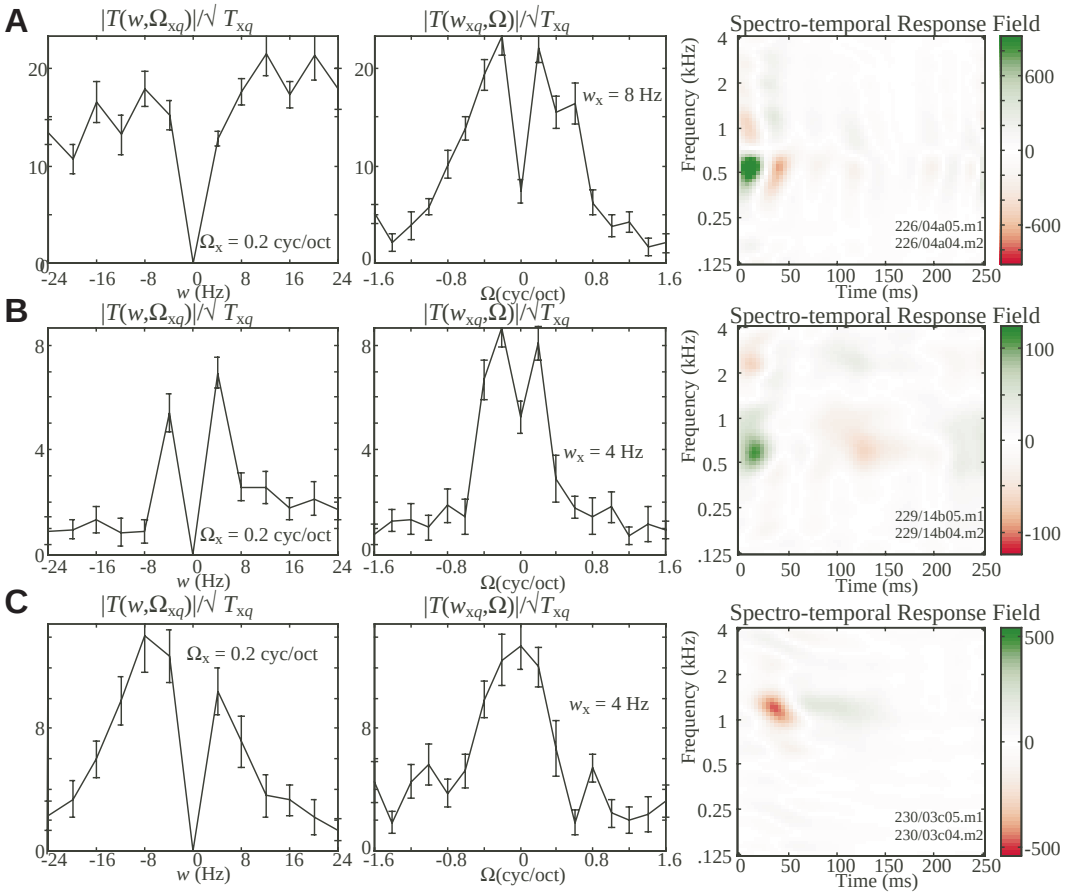

Figure 10: Further examples of Spectro-temporal transfer function sections, corresponding STRFs. Conventions as in Fig. 8. **A**: fast dynamics **B**: slow dynamics **C**: offset response.

cluding the inhibitory surrounds) is parameterized by $x_{m_\pm}$ (Eq. 11), a measure which correlates well with the BF as shown visually in Figs. 6 and 8–10, and quantitatively in Fig. 12A.

In many cases, the inhibitory surround is spectrally asymmetric around the BF (Fig. 9C); such asymmetry is effectively captured by the parameter ϕ (Eq. 12), where ϕ values near zero indicate roughly symmetric STRFs, while $\phi \approx 90°$ indicate strong inhibition below the BF, and $\phi \approx$ -90° indicate strong inhibition above below the BF. The ϕ distribution in our sample is summarized in Fig. 12C. It closely resembles that seen earlier with downward moving and stationary ripples

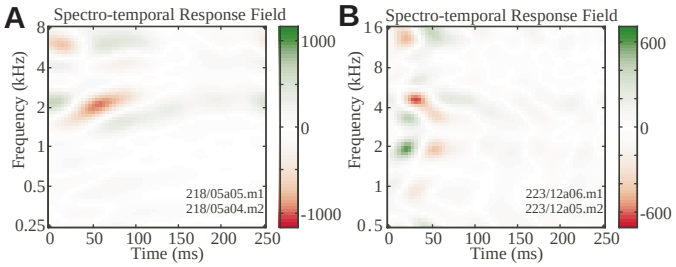

Figure 11: Two cells with unusual receptive fields.

(Kowalski et al. 1996a; Versnel et al. 1995; Schreiner and Calhoun 1995).

STRFs also vary considerably in their temporal dynamics, best seen in the t–x domain. Some are fast with envelopes that decay relatively rapidly (Figs. 9C and 10A). Others are slow, taking over 150 ms to decay (as in Figs. 9A and 10B). These response dynamics reflect details of the temporal transfer function such as the ripple velocity at which it peaks (characteristic ripple velocity) and its width (ripple velocity bandwidth). STRFs also exhibit an onset delay (or latency) which is captured by the $\tau_{d_\pm}$ value derived from the phase function (Eq. 11). The distribution of this delay tends to be well clustered around 25 ms as seen in Fig. 12B . Finally, unit STRFs can be generally classified as either *onset* (Figs. 9A–C, 10A–B, most cells) or *offset* (Fig. 10C), a property which corresponds, respectively, to the negative or positive sign of the parameter θ. Onset STRFs are far more common in our sample as seen in the θ distribution in Fig. 12C.

Finally, STRFs may display very complex dynamics and spectro-temporal selectivity that are not easily captured by simple parameters. Two examples of such STRFs are shown in Fig. 11. One might be tempted to dismiss such STRFs as mere aberration or noise, except for the fact that they are derived from repeatable responses (δ = 0.10 and ϵ = 0.49 for Fig. 11A and δ = 0.03 and ϵ = 0.04 for Fig. 11B).

3.2 Separability and its relation to STRF shape

Separability is an important property of the transfer functions which has significant experimental and theoretical implications. In this paper, we assume quadrant separability, and ask whether responses are fully separable, the degree of inseparability, and the origin of the inseparability. Each of these indicators has a potentially useful interpretation for the shape of the STRF, and the underlying structure

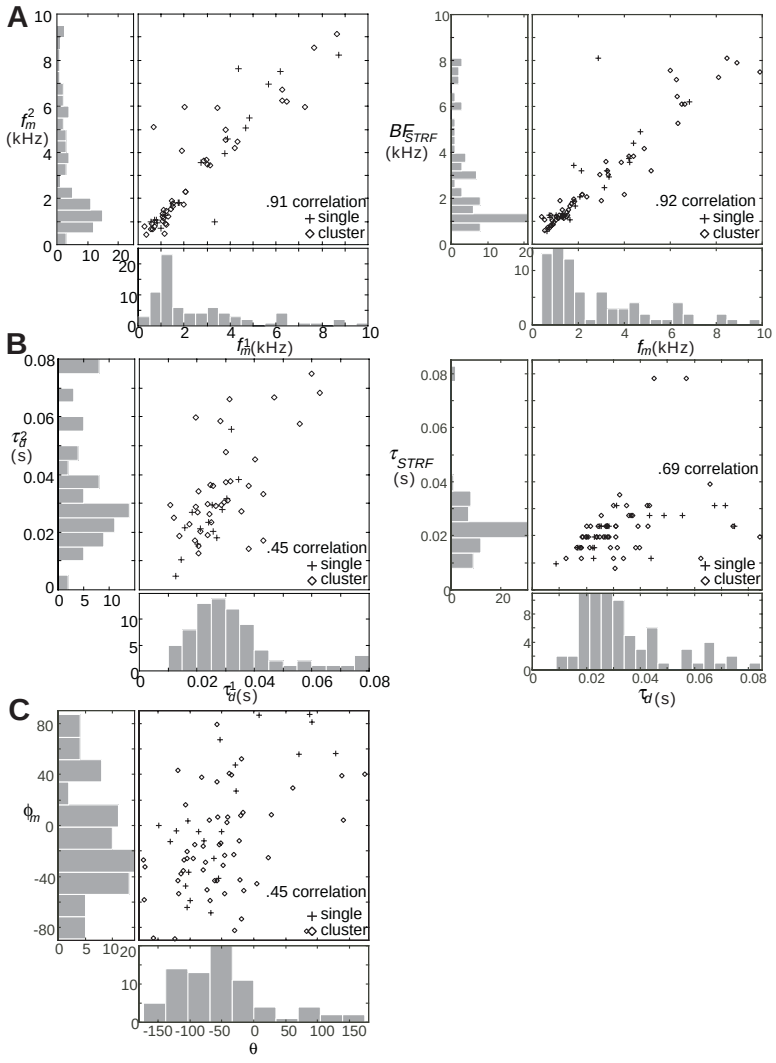

Figure 12: The statistical distribution of parameters. **A**: (left) f_m^1 vs. f_m^2, i.e., center frequency f_m as determined by quadrant 1 vs. quadrant 2; (right) f_m vs. BF_{STRF}, i.e., quadrant averaged center frequency f_m vs. frequency giving highest STRF peak. **B**: (left) τ_d^1 vs. τ_d^2, i.e., mean delay τ_d as determined by quadrant 1 vs. quadrant 2; (right) τ_d vs. τ_{STRF}, i.e., quadrant averaged mean delay τ_d vs. delay giving highest STRF peak. **C**: temporal phase θ vs. spectral phase ϕ_m.

of processes that give rise to it.

The simplest and most general way to examine full separability is to compute

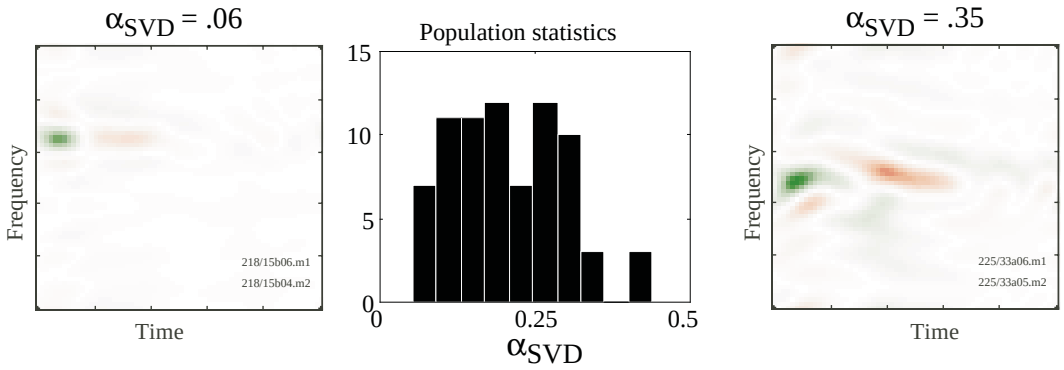

Figure 13: A small and a large α_{SVD} cells, with the distribution of α_{SVD} in the middle.

the SVD matrix Λ (Eq. 6), and examine the number and value of the resulting singular values. Fig. 13 illustrates the distribution of $\alpha_{SVD} = (1 - \lambda_1^2/(\sum_i \lambda_i^2))$ computed from all the cells used. Values near 0 indicate that only the first singular value has a large non-zero value, and hence a fully separable STRF. Increasing values indicate increasing degree of inseparability.

As can be seen from Fig. 13, a significant fraction are inseparable, but with no indication as to the origin of the inseparability. Specifically, it can be shown that fully separable transfer functions must have symmetric transfer function magnitudes about the (w, Ω) origin. Thus, inseparability may be due to a combination of three factors (Eqs.7,8,9):

- α_d, the imbalance in response directionality or in overall strength of the responses to the upward and downward moving ripples;
- α_t, the asymmetry in the temporal transfer function $F(w)$;
- α_s, the asymmetry in the spectral transfer function $G(\Omega)$.

The distribution of these three parameters is shown in Fig. 14. The directionality parameter α_d is distributed approximately normally between negative and positive values. This parameter is closely related to the directional selectivity of the STRF. STRFs with large $|\alpha_d|$ values exhibit obvious directional shapes such as seen in Fig. 14 (top center). A significant proportion of units (37%) also have spectral dissimilarity values (α_s) exceeding 0.3. An STRF with especially large

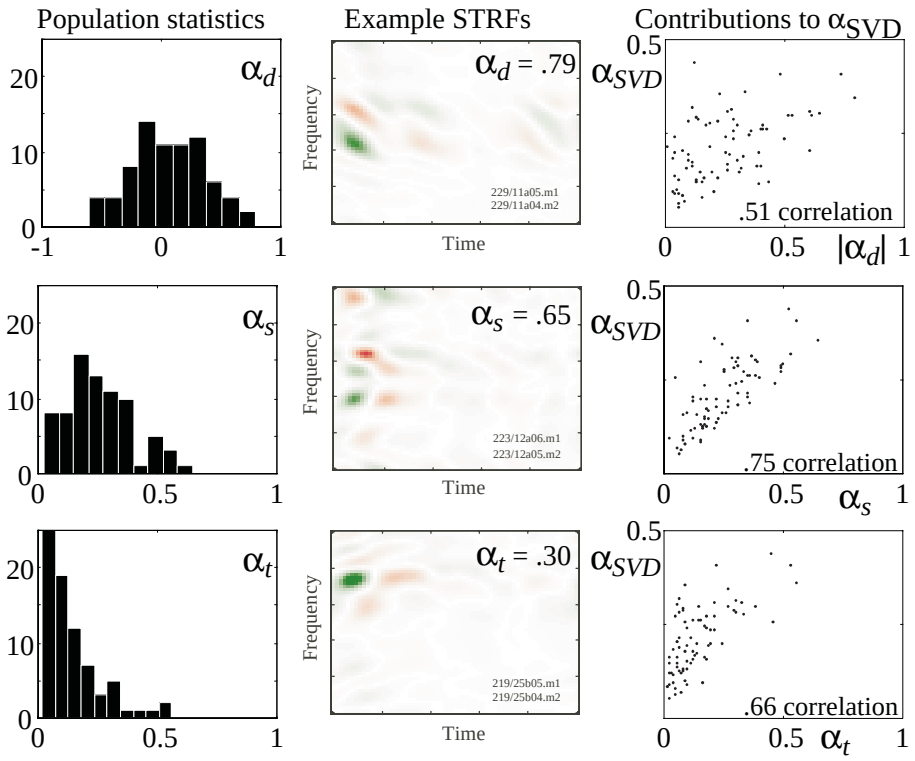

Figure 14: (left) The distribution of three inseparability indicators, α_t, α_s and α_d; (center) examples of STRFS with extreme values of the corresponding inseparability indicator; (right) distributions of each inseparability indicator, plotted against total inseparability, α_{SVD}.

α_s is shown in Fig. 14 (middle center). Note that these STRFs may not necessarily exhibit obvious directionally selective shapes.

A strikingly different finding is the dearth of units (12%) with significant temporal dissimilarity ($\alpha_t > 0.3$) as seen in the distribution in Fig. 14 (bottom left). An STRF with $\alpha_t = 0.30$ is displayed in Fig. 14 (bottom center): it is difficult to detect simple correlates of the large α_t values in the shape of the STRF.

The three inseparability indicators do not appear to be significantly correlated, based on the pair-wise scatter plots in Fig. 15, suggesting that independent mechanisms underlie the expression of each factor. By contrast, each factor (as expected) is well correlated with the total SVD index as seen in Fig. 14 (right column).

We can define a composite measure of inseparability, the mean of α_t, α_s and

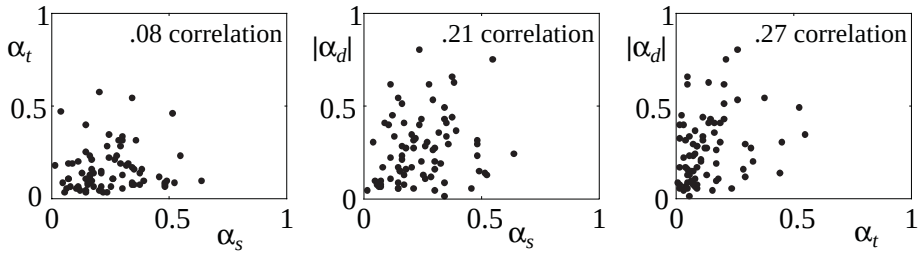

Figure 15: The correlation of three inseparability indicators, α_t, $\alpha_s$and α_d.

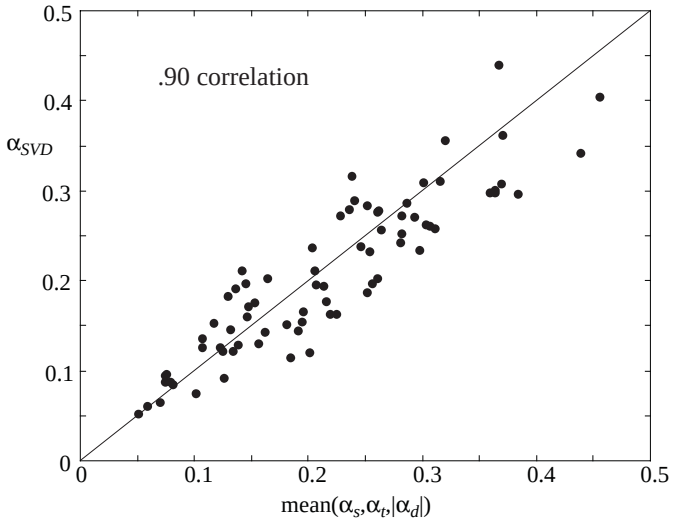

Figure 16: The correlation between the mean of α_t, α_s and α_d and α_{SVD}.

$|\alpha_d|$. Fig. 16 illustrates that this measure is highly correlated to α_{SVD}, and hence is an equally valid measure of inseparability.

4 Discussion

4.1 Summary of results

The emphasis in this work has been on presenting a technique to describe neural response patterns of units in the cortex. More precisely, we use moving ripples to

characterize the spectral and temporal properties of responses of auditory cortical neurons, although this is a general method that can be used anywhere responses are shown to be substantially linear for broadband stimuli.

We have examined the nature of AI responses to rippled spectra moving in both upward and downward directions, and incorporated these responses into the STRF. A summary of the main results include:

- We confirm earlier findings (Kowalski et al. 1996a), that AI units respond in a phase-locked fashion to the moving ripples over a range of velocities and directions that depend on the ripple density of the spectrum. In particular, responses are usually tuned around a specific ripple velocity and density. In the ferret, responses are commonly best in the 4-16 Hz range and densities lower than 2 cycles/octave. These findings are roughly consistent with those found in different species using different experimental paradigms: experiments with dynamic spectra (e.g., narrowband such as AM and FM tones, or broadband such as modulated noise and click trains) have found similar maximum rates of synchronized responses in AI (Schreiner and Urbas 1988; Eggermont 1994).

- We demonstrate a similarity between responses to upward and downward-moving ripples. Specifically, the response parameter values and distributions to either direction are comparable (even if unequal), and hence reflect general dynamic response properties, not direction-specific properties *per se*.

- Bi-directional spectro-temporal transfer functions are measured that exhibit a rich variety of shapes and cover a wide range of stimulus parameters. The STRF describes the way AI units integrate stimulus power along the spectro-temporal dimensions.

- We illustrate a variety of STRFs with a broad range of BFs, bandwidths, asymmetrical inhibition, temporal dynamics, and orientation selectivity. We have assessed the prevalence of these features over all sampled units by examining the distribution of specific parameters that reflect each of these features.

- The degree and origin of inseparability of the unit transfer functions is assessed using two methods. In the first, SVD analysis is applied on the entire (bi-directional) transfer function to determine the number and ratio of the

resulting singular values. The results indicate that AI units span a relatively uniform distribution between full separability to moderate inseparability. In the second method, we examine the origin of inseparability and find that it is primarily due to two factors: imbalance in the response power and an asymmetry in the spectral transfer function relative to the direction of ripple motion. Interestingly, we find that temporal (and not spectral) transfer functions are relatively symmetric, and hence contribute little to overall transfer function inseparability.

4.2 Separability and its implications

An important property of the responses is that, for ripples moving in only one direction, the spectral and temporal functions are separable: within each quadrant they can be measured independently of each other. The property of quadrant separability makes it possible to measure the overall spectro-temporal transfer function in reasonable times using only single ripples since only a few velocity and spectral density combinations need to be measured. We have established (Kowalski et al. 1996a; Klein et al. 2000) that all recorded transfer functions in AI exhibit quadrant separability. In the experiments reported here, we assumed quadrant separability (Kowalski et al. 1996a; Kowalski et al. 1996b), and proceeded to examine whether the resulting two-dimensional transfer functions are fully-separable. Our findings indicate that AI responses fall uniformly on a continuum between moderately to fully-separable.

A fully separable cell cannot be directionally selective in its responses; inseparability is a necessary condition for the formation of more complex STRFs. One possible consequence of inseparability is orientation selectivity. An orientation-selective STRF usually has a distinctive elongated form along a spectro-temporal direction that matches that of its most sensitive ripple stimulus. For example, the STRF illustrated in Fig. 8B is most responsive to a ripple $\Omega = 0.4$ cyc/oct, $w = -4$ Hz, whose spectrogram matches well the outline of the STRF spacing and orientation. Orientation selectivity implies that a unit is differentially responsive to one direction of ripple movement, and hence must have a significant non-zero directionality index ($\alpha_d = 0.79$). Therefore, orientation selectivity necessarily implies an inseparable STRF. The opposite is not true: an inseparable STRF might reflect other factors such as asymmetric temporal and/or spectral transfer functions (α_t or $\alpha_s \neq 0$) which do not manifest themselves in an obvious elongated form or preferential responses to one direction or another (as shown in Fig. 14, center column, middle and bottom).

Separability also places strong constraints on the underlying biological processes that give rise to the STRF shapes. For example, full separability suggests that the STRF is constituted of independent temporal and spectral processing stages. By contrast, inseparability (or just quadrant separability) implies spectrally and temporally intertwined stages of processing with the specific form of the model being entirely dependent on the details of the transfer functions. Quadrant separability in particular is a very strong constraint on both the neural inputs and the processing of the unit: almost all neural networks (whether linear or non-linear) with multiple fully-separable STRFs as inputs, will in general produce a totally inseparable STRF. In particular, the naive procedure of constructing a directionally sensitive STRF by taking the simple sum of two fully separable STRFs with differing f_m and τ_d will produce a totally inseparable STRF which is not quadrant separable. To produce a quadrant separable STRF requires special inputs and/or special processing.

In (Simon et al. 1999b), it is shown that a quadrant separable, temporally symmetric (i.e., $\alpha_t \ll 1$), cortical neuron can be easily constructed by taking inputs from (potentially) many units with (potentially) different spectral response fields and even with (potentially) different temporal impulse response properties, as long as the temporal dynamics of the inputs to the cortical cell are fast compared to the temporal dynamics of the cortical cell itself. This would occur for instance if the inputs were temporally phase-lagged relative to each other (though not necessarily 90° as in Saul and Humphrey (1990) and Dong and Atick (1995).

This is consistent with the input neural connectivity one expects from layer IV cortical neurons, which receive input from thalamic Medial Geniculate Body (MGB). MBG neurons may have fully separable STRF (as is the case for typical Inferior Colliculus Central (ICC) neurons (Escabi and Schreiner 1999)), with different spectral response fields (differing in width, extent/location of inhibitory bands, and to a lesser extent, best frequency). MGB temporal cross-sections of transfer functions are essentially constant when low-passed at a cut-off frequency appropriate to cortical behavior (e.g., typically well below 100 Hz) (Yeshurun et al. 1985). Furthermore, some MGB neurons may have a temporal phase-lag, as in the visual system's Lateral Geniculate's "lagged cells") (Saul and Humphrey 1990).

Significantly, the property of quadrant separability with temporal symmetry does not allow for any cortical inputs unless those inputs have the same temporal behavior as the neuron studied. If, for instance, all neurons in the same cortical column have similar temporal properties, including similar neural delays, this would be consistent with quadrant separability. Otherwise, cortical inputs would

break quadrant separability and create a totally inseparable neuron. Total inseparability would be expected for cortical neurons in layers which receive significant input from other cortical columns, or from any other neural source with significantly different temporal processing, including (but not limited to) any significant delays.

It is possible that this extremely constraining result is an anesthesia-induced effect. If not, the result is a fascinating constraint on the neural network providing input to a given cortical cell.

5 Acknowledgements

This work is supported by a MURI grant N00014-97-1-0501 from the Office of Naval Research, a training grant NIDCD T32 DC00046-01 from the National Institute on Deafness and Other Communication Disorders, and a grant NSFD CD8803012 from the National Science Foundation. We would particularly like to thank Alan Saul. We also thank Jos Eggermont, Izumi Ohzawa and Malcolm Slaney for very helpful and illuminating discussions.

References

Aertsen, A. M. H. J. and P. I. M. Johannesma (1981). The spectro-temporal receptive field: A functional characteristic of auditory neurons. *Biol. Cybern.* 42, 133–143.

deCharms, R. C., D. T. Blake, and M. M. Merzenich (1998). Optimizing sound features for cortical neurons. *Science* 280, 1439–1443.

Depireux, D. A., J. Z. Simon, and S. A. Shamma (1998). Measuring the dynamics of neural responses in primary auditory cortex. *Comments in Theoretical Biology* 5(2), 89–118.

Dong, D. and J. J. Atick (1995). Temporal decorrelation: a theory of lagged and nonlagged cells in the lateral geniculate nucleus. *Network: Computation in Neural Systems* 6, 159–178.

Efron, B. and B. Tibshirani (1993). *An Introduction to the Bootstrap*. New-York: Chapman and Hall.

Eggermont, J. J. (1993). Wiener and Volterra analyses applied to the auditory system. *Hearing Res.* 66, 177–201.

Escabi, M. A. and C. E. Schreiner (1999). Non-linear spectro-temporal envelope processing in the cat ICC. *Assoc. Res. Otolaryngology Abstr.* 22, 869.

Evans, E. F. (1979). Single-unit studies of mammalian cochlear nerve. In H. A. Beagley (Ed.), *Auditory investigations: the scientific and technological basis*, Volume 68, Oxford, UK, pp. 324–367. Clarendon.

Ghiglia, D. C. and M. D. Pritt (1998). *Two-dimensional phase unwrapping : theory, algorithms, and software*. New York, NY: Wiley-Interscience.

Haykin, S. S. (1988). *Digital communications*. New York, NY: Wiley.

Klein, D. J., D. A. Depireux, J. Z. Simon, and S. A. Shamma (1999). Robust spectro-temporal reverse correlation for the auditory system: Optimizing stimulus design. *J. Comput. Neurosci.* to appear.

Klein, D. J., J. Z. Simon, S. A. Shamma, and D. A. Depireux (2000). Measuring the dynamics of neural responses in ferret primary auditory cortex using TORCS. *J. Neurophysiol.* in preparation.

Kowalski, N., D. A. Depireux, and S. A. Shamma (1996a). Analysis of dynamic spectra in ferret primary auditory cortex: I. Characteristics of single unit responses to moving ripple spectra. *J. Neurophysiol.* 76(5), 3503–3523.

Kowalski, N., D. A. Depireux, and S. A. Shamma (1996b). Analysis of dynamic spectra in ferret primary auditory cortex: II. Prediction of unit responses to arbitrary dynamic spectra. *J. Neurophysiol.* 76, 3524–3534.

Kvale, M. and C. E. Schreiner (1995). Perturbative m-sequences for auditory systems identification. *Acustica* 81.

Mendelson, J. R., C. E. Schreiner, M. L. Sutter, and K. L. Grasse (1993). Functional topography of cat primary auditory cortex: responses to frequency-modulated sweeps. *Exp. Brain. Res.* 94, 65–87.

Middlebrooks, J. C., R. W. Dykes, and M. M. Merzenich (1980). Binaural response-specific bands in primary auditory cortex of the cat: topographical organization orthogonal to isofrequency contours. *Brain Res.* 181, 31–48.

Nelken, I., Y. Prut, E. Vaadia, and M. Abeles (1994). Population responses to multifrequency sounds in the cat auditory cortex: One- and two-parameter families of sounds. *Hearing Res.* 72, 206–222.

Papoulis, A. (1962). *The Fourier integral and its applications*. New York, NY, USA: McGraw-Hill.

Politis, D. N. (1998). Computer-intensive methods in statistical analysis. *IEEE signal processing magazine* 15(1), 39–54.

Reale, R. A. and T. J. Imig (1980). Tonotopic organization in auditory cortex of the cat. *J. Comp. Neurol.* 192, 265–291.

Saul, A. B. and A. L. Humphrey (1990). Spatial and temporal response properties of lagged and nonlagged cells in cat lateral geniculate nucleus. *J. Neurophysiol.* 64, 206–224.

Schreiner, C. E. and B. M. Calhoun (1995). Spectral envelope coding in cat primary auditory cortex: Properties of ripple transfer functions. *J. Aud. Neurosci.* 1, 39–61.

Schreiner, C. E., J. Mendelson, and M. L. Sutter (1992). Functional topography of cat primary auditory cortex: representation of tone intensity. *Exp. Brain Res.* 92, 105–122.

Schreiner, C. E. and M. L. Sutter (1992). Topography of excitatory bandwidth in cat primary auditory cortex: single-neuron versus multiple-neuron recordings. *J. Neurophysiol.* 68, 1487–1502.

Shamma, S. A., J. W. Fleshman, P. R. Wiser, and H. Versnel (1993). Organization of response areas in ferret primary auditory cortex. *J. Neurophysiol.* 69, 367–383.

Shamma, S. A., H. Versnel, and N. Kowalski (1995). Ripple analysis in ferret primary auditory cortex: I. Response characteristics of single units to sinusoidally rippled spectra. *J. Aud. Neurosci.* 1, 233–254.

Simon, J. Z., D. J. Klein, S. A. Shamma, and D. A. Depireux (1999a). Measuring the dynamics of neural responses in ferret primary auditory cortex: II. Prediction of responses to complex moving ripple spectra.

Simon, J. Z., D. J. Klein, S. A. Shamma, and D. A. Depireux (1999b). Temporal symmetry and quadrant separability: Theory and implications for biological network connectivity.

Sutter, M. L., W. C. Loftus, and K. N. O'Connor (1996). Temporal properties of two-tone inhibition in cat primary auditory cortex. *Assoc. Res. Otolaryngology Abstr.* 19, 452.

Theunissen, F. E., K. Sen, and A. J. Doupe (1999). Spectral-temporal receptive fields of non-linear auditory neurons obtained using natural sounds. *J. Neurosci.* in press.

Versnel, H., N. Kowalski, and S. A. Shamma (1995). Ripple analysis in ferret primary auditory cortex: III. topographic distribution of ripple response parameters. *J. Aud. Neurosci.* 1, 271–285.

Watson, A. B. and A. J. Ahumada (1985). Model of human visual-motion sensing. *J. Opt. Soc. Am. A* 2(2), 322–341.

Yeshurun, Y., Z. Wollberg, N. Dyn, and N. Allon (1985). Identification of MGB cells by volterra kernels. I. prediction of responses to species specific vocalizations. *Biol. Cybern.* 51(6), 383–90.